

# Constraining Torus Models for AGNs Using X-Ray Observations

E. Ibar<sup>1,2</sup> and P. Lira<sup>1</sup>

<sup>1</sup> Departamento de Astronomía, Universidad de Chile, Camino del Observatorio 1515, Santiago, Chile.

<sup>2</sup> Institute for Astronomy, University of Edinburgh, The Royal Observatory, Edinburgh, Scotland, EH9 3HJ.  
e-mail: ibar@roe.ac.uk

Received...; accepted...

## ABSTRACT

**Context.** In Unification Models, Active Galactic Nuclei (AGNs) are believed to be surrounded by an axisymmetric structure of dust and gas, which greatly influences the observed properties of the AGNs according to the direction from which they are observed.

**Aims.** In this paper, the distribution of the column densities as observed by *Chandra* in the GOODS fields, and the spectral index of the Cosmic X-Ray Background (CXR) in the 2 – 10 keV range, are used to determine geometrical constraints for already proposed torus models.

**Methods.** The models are computed assuming a direct relationship between the inclination angle and the optical depth in the line of sight, Ueda's AGN luminosity function, and a template for the AGN emission. The models can describe the wide range of observed column densities,  $20 \leq \log(N_H \text{ cm}^{-2}) \leq 25$ . Biases arising from the flux limit reached by *Chandra* in the GOODS fields ( $F_{2-8\text{keV}}^{\text{limit}} \approx 10^{-16} \text{ erg sec}^{-1} \text{ cm}^{-2}$ ) and the limit for reliable optical spectroscopic redshifts above  $R \sim 24$  are taken into account.

**Results.** It is found that the best torus model is given by an exponential angle dependency, such as that given by Granato & Danesse in 1994.

**Conclusions.** The dependency of the opening angle of the matter density distribution is strongly constrained by the observed column densities, while the CXR spectral index indicator gives constraints through the Type II/I AGN fraction only. We conclude that besides the fraction of Compton Thick sources predicted by our torus models, the inclusion of a local Compton Thick population is required to fit the CXR at  $E > 20 \text{ keV}$ .

**Key words.** Galaxies:active – Galaxies:structure – X-rays:general – X-rays:diffuse background

## 1. Introduction

A unified scheme to explain a variety of Active Galactic Nuclei (AGNs) has been proposed by Antonucci (1993) based on Seyfert galaxies, a class of local active galaxies. According to this *Unification Model*, the active nucleus is surrounded by a dusty toroidal structure, usually called a torus, composed of gas and dust, which determines dramatic spectral differences depending on our line of sight towards the central source. In the X-Ray domain, if an AGN has a neutral Hydrogen column density ( $N_H$ ) in the line of sight smaller (viewed face-on) or greater (edge-on) than  $10^{22} \text{ cm}^{-2}$ , then the object is classified as Type I or Type II, respectively.

This dusty toroidal structure absorbs the optical, ultraviolet and soft X-Ray emission from the active nucleus. However, hard X-Ray photons ( $> 2 \text{ keV}$ ) can partially escape from the cold material. Therefore, from X-Ray observations, it is possible to measure the column density in the line of sight, and put tight constraints on the properties of the obscuring medium.

It is commonly believed that the observed X-Rays coming from AGNs are produced in the innermost regions near the super-massive black hole, the corona, where low energy photons from the accretion disk are reprocessed by energetic elec-

trons (either mildly relativistic thermal electrons or highly relativistic non-thermal electrons) via Inverse Compton Scattering. The main result of this process is an observed spectral energy distribution described by a power law, with a typical slope  $\Gamma \approx 1.9$  (Nandra & Pounds 1994), and an exponential cutoff energy at  $\approx 300 \text{ keV}$  (Matt et al. 1999). The radiation can also be reflected or/and scattered depending on the circumnuclear material distribution causing the overall spectral shape to be considerably flatter,  $\Gamma \approx 1.7$ , and an apparent smaller cutoff energy (see Svensson 1996).

Since Compton Thin AGNs (those with  $N_H < 10^{24} \text{ cm}^{-2}$ ) are ubiquitous emitters in the hard X-Ray band (2 – 10 keV), deep X-Ray surveys have proven to be the best way to estimate the number density and evolution of active galaxies in the Universe (Mushotzky 2004). On the other hand, detections in the soft X-Ray band (0.5 – 2 keV) can miss even moderately absorbed sources and are usually contaminated by thermal sources such as Galactic diffuse emission, heliospheric and geocoronal diffuse components, intergalactic warm gas, and from star-burst galaxies (Markevitch et al. 2003).

As hard X-Ray energy photons can penetrate the surrounding material, and eventually escape from the AGN host, they

can be detected with the present generation of X-Ray telescopes. But, if the Hydrogen column density along the line of sight becomes larger than the inverse of the photoelectric Cross Section  $\sigma_{10\text{keV}}^{-1} \approx 10^{24} \text{ cm}^{-2}$  (see Matt 2002), then the medium becomes Compton Thick ( $\tau = N_H \sigma \approx 1$ ). In this case, the only observable emission component is coming from photons scattered and/or reflected by the circumnuclear media (Wilman & Fabian 1999).

Since in AGNs with  $N_H > 10^{22} \text{ cm}^{-2}$  the direct nuclear emission is highly absorbed, these sources have a hard X-Ray energy distribution (harder than typical unobscured AGN) that can be used to model the hard spectrum of the observed Cosmic X-Ray Background (CXRIB) at  $E < 20 \text{ keV}$  ( $\Gamma_{2-10\text{keV}}^{\text{CXRIB}} \approx 1.4$ ). One caveat, however, is that the CXRB spectrum would combine the torus obscuration properties and the cosmic evolution of the intrinsic AGN emission. Hence we must know in advance the range of AGN redshifts and luminosities (in other words, a precise AGN luminosity function) to evaluate a reliable synthetic spectra and deduce some torus properties from the CXRB. Unfortunately, deep X-Ray surveys used to study the distribution of AGNs in the Universe are always flux limited (nowadays  $F_{2-10\text{keV}}^{\text{limit}} \approx 10^{-16} \text{ erg sec}^{-1} \text{ cm}^{-2}$ ), and therefore biased against fainter sources. In fact, the population of high redshift low luminosity and low redshift highly obscured AGNs is still not well known. This problem translates into a poorly determined faint end of the luminosity function, implying uncertainties in the contribution of obscured AGNs to the CXRB. This problem is more relevant if a large population of highly absorbed AGNs (Compton Thick sources) is needed to fit the observed CXRB spectrum.

The aim of this work is to constrain different torus geometries that can reproduce the observed distribution of Hydrogen column densities in AGNs obtained by *Chandra* in the GOODS fields. We also extrapolate our torus models to fit the CXRB spectrum which can give further constraints, basically using the observed slope in the  $2 - 10 \text{ keV}$  band.

Section 2 shows the observational data which were used in our analysis. In Section 3 we explain the theoretical modelling and in Section 4 we present our models and obtained results. In Section 5 we explain how we predicted the CXRB emission using our torus models and the results coming from this analysis. In Section 6 our results are discussed and we present the conclusions in Section 7. Throughout this work we use:  $\Omega_m = 0.3$ ,  $\Omega_\Lambda = 0.7$  and  $H_0 = 70 \text{ km sec}^{-1} \text{ Mpc}^{-1}$  (Spergel et al. 2003).

## 2. Deep X-Ray Observations

### 2.1. AGNs in the Great Observatories Origins Deep Survey

In the past few years, many deep *Chandra* images of the extragalactic sky have been obtained, with the  $2 \text{ Ms}$  *Chandra* Deep Field-North (CDF-N; Alexander et al. 2003) and  $1 \text{ Ms}$  *Chandra* Deep Field-South (CDF-S; Giacconi et al. 2002) being the two deepest ( $F_{2-10\text{keV}}^{\text{limit}} \approx 1.4 \cdot 10^{-16} \text{ erg s}^{-1} \text{ cm}^{-2}$  for CDF-N and only a factor 2 shallower for CDF-S). These two fields contain within them the Great Observatories Origins Deep Survey (GOODS) fields, GOODS-North and GOODS-

South. The optical counterparts to the X-Ray sources yield the spectroscopic redshift of the sources. A detailed explanation of the multi-wavelength observations in the GOODS fields can be found in Treister et al. (2004).

From the total number of observed X-Ray sources (selecting only those detected within the hard X-Ray  $2 - 10 \text{ keV}$  band) in the GOODS fields, 210 in the North and 141 in the South, only approximately 10% do not have an optical identification (an optical counterpart within  $\sim 1''$  of the X-Ray centroid). The optical counterpart yields an unambiguous number of 178 AGNs in GOODS-N and 128 in GOODS-S. Of these sources, 103 in GOODS-N and 82 in GOODS-S have spectroscopically determined redshifts (Barger et al. 2003; Szokoly et al. 2004), which are useful to determine the Hydrogen column density,  $N_H$ , in the line of sight.

### 2.2. Observed Column Densities

To deduce  $N_H$  for each source, the Hardness Ratio  $HR = (H - S)/(H + S)$  is used (Alexander et al. 2003; Giacconi et al. 2002), where  $S$  is the photon number counts detected in the soft X-Ray band ( $0.5 - 2 \text{ keV}$ ), and  $H$  is the photon number counts in the hard X-Ray band ( $2 - 8 \text{ keV}$ ). Assuming a template for the AGN emission (Figure 2, see Subsection 3.1 for details) and knowing the redshift from the optical counterpart, it is possible to estimate the Hydrogen column density along the line of sight by comparing the observed  $HR$  with the predicted one. Since this analysis is not very sensitive to small  $N_H$  values and tends to overestimate the minimum assumed  $N_H$  ( $10^{20} \text{ cm}^{-2}$ ), we randomly assigned values between  $N_H = 1 - 3 \cdot 10^{20} \text{ cm}^{-2}$  to those sources. The deduced distribution is presented in Figure 1.

By far, the largest assumption when deriving column densities from the observed Hardness Ratios (assuming that accurate redshifts for the sources are available, as is the case for the GOODS AGN), is the adopted spectral shape. Previous work have assumed that all AGN can be parameterized by an absorbed power law with a unique Gamma index. However, it is clear that the presence of reflection, and reprocessed emission is necessary to explain the CXRB, hence the assumption of a complex template changes the slope of the X-Ray continuum and  $N_H$  predictions. We predict the outgoing X-Ray spectral shape in different directions assuming a geometrical density distribution for the torus. Since our models change the amount of obscuration along the line of sight in a well predicted manner, this information has been used to derive the observed  $N_H$  values in a *consisting way* for each torus model.

From our results, the fraction of Type II ( $N_H > 10^{22} \text{ cm}^{-2}$ ) over the total number of 185 sources observed by *Chandra* in the GOODS fields is  $\sim 0.5$ . The observed fraction Type II/I does not show a clear dependency on the redshift or luminosity. The absence of high luminosity sources in the GOODS fields generates this result, as discussed in Treister et al. (2005).

## 3. Model General Properties

We first assume that the X-Ray emission in AGNs comes from the nearest region to the super-massive black hole. This re-

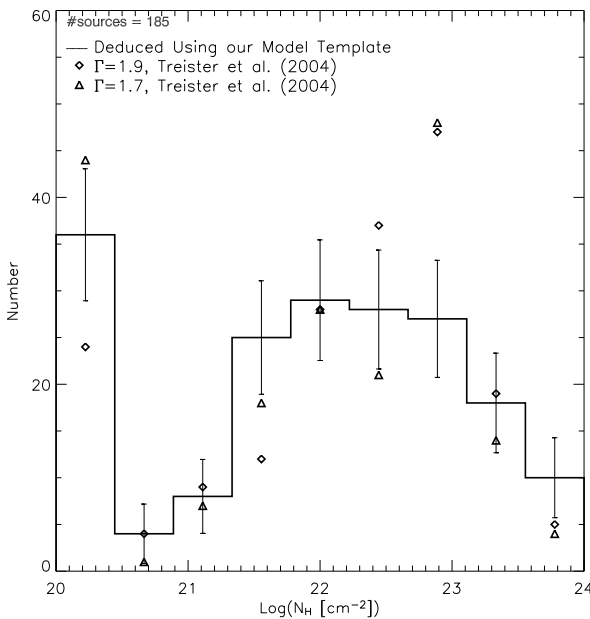


**Fig. 1.** Distribution of the Hydrogen column densities derived for 185 AGNs observed by *Chandra* in the GOODS fields (Treister et al. 2004). All sources have determined spectroscopic redshift from Szokoly et al. (2004) and Barger et al. (2003). The  $N_H$  values are deduced using the *Hardness Ratio* (Giacconi et al. 2002; Alexander et al. 2003), an assumed spectral energy distribution (Subsection 3.1) and the redshift from the optical counterpart. Error bars are estimated using poissonian statistics for small numbers given by Gehrels (1986). A comparison with previous Treister et al.(2004) results is also shown. *Data given by E. Treister.*

gion has a typical scale of  $R_C \approx 10 - 100 R_S$  (Where  $R_S = GM_{BH}/c^2$  is the Schwarzschild Radius), implying spatial scales of  $R_C \approx 10^{-4} - 10^{-3}$  pc for a typical super-massive black hole of  $M_{BH} \approx 10^8 M_\odot$ . Previous torus models (see Figure 5), constrained by infrared spectroscopic observations, suggest sizes from  $\sim 1$  pc to  $\sim 100$  pc. Therefore, for all practical purposes we can consider the X-Ray source as a point-like emitting region, implying an easy treatment for the X-Ray radiation that will provide the total column density along the line of sight.

### 3.1. The AGN Template

With the observations of X ray satellites like GINGA, ASCA, and BeppoSAX, different spectral components have been recognized in the X ray spectra of AGNs. We modelled the observed Spectral Energy Distribution (SED) from each point source as:

$$F_E = \frac{dF}{dE}(L_X, z, N_H, \Gamma) = A \frac{L_X(1+z)}{4\pi d_L^2(z)} \left( e^{-\sigma(E_z)N_H} + \text{REF\%} \right) \times \left( E_z^{-\Gamma+1} e^{-E_z/E_C} + \text{REP}(E_z) \right) \quad (1)$$

where  $E_z = E(1+z)$ ,  $A$  is a normalization value so that  $L_X$  corresponds to the intrinsic integrated luminosity in the  $2 - 10$  keV rest-frame band (to be used together with the luminosity function),  $z$  is the redshift,  $d_L(z)$  is the luminosity distance parameterized by the assumed cosmology,  $\sigma(E)$  is the effective cross section for a solar metallicity medium (Morrison & McCammon 1983) extrapolated to higher energies ( $\gtrsim 10$  keV) by a photoelectric bound-free cross section  $\propto E^{-3}$  (note that when  $\text{Log}(N_H \text{ cm}^{-2}) > 24$ , Compton recoil, or Compton down scattering, becomes important at high energies). A spectral index  $\Gamma = 1.9$  is used to characterize the primary emission, according to the overall results from spectral analysis of nearby active galaxies (Nandra & Pounds 1994) and with the mean value in the Lockman Hole observed by *XMM-Newton* (Mainieri et al. 2002). The high energy cut-off  $E_C \approx 300$  keV is adopted from bright Seyfert galaxies and it becomes important for predicting the contribution of AGNs to the CXRB above 10 keV (Ueda et al. 2003), although this value is highly unconstrained (Matt et al. 1999).  $\text{REP}(E)$  is the estimated angle averaged reprocessed primary emission by Compton cold (disk) reflection, assuming a solid angle of  $2\pi$  and solar abundances for all elements (dashed line from Figure 5 in Magdziarz & Zdziarski 1995). The ratio of the reflection component  $\text{REP}(E)$  to the primary one is about 10% just below 7.1 keV (the K edge energy of cold iron atoms) and rapidly decreases toward lower energies (0.1% at 1 keV), while above 7.1 keV it has a maximum of about 70% around 30 keV. Compton down scattering becomes important at  $N_H > 10^{24} \text{ cm}^{-2}$  affecting the high energy X ray photons through electron recoil, as described by Wilman & Fabian (1999). For simplicity, in this work, we have not considered the  $K\alpha$  line component from the ionized iron atoms, whose contribution is less than a few percent in the hard X ray band (2 – 10 keV). Finally, we added a reflected  $\text{REF\%} = 2\%$  component from the central emission produced by warm ionized gas located above the opening angle torus. The template for different column densities can be seen in Figure 2.

### 3.2. Torus Properties

We modelled the obscuring region, the torus, as a simple axisymmetrical matter distribution surrounding the accretion disk. The torus produces different amounts of absorption depending on the line of sight, which can also be treated as different optical depths. We assume a solar abundance for the torus, using the photoelectric cross section given by Morrison & McCammon (1983), and a standard Galactic *Gas-to-Dust* ratio  $N_H/E(B-V) = 5.8 \cdot 10^{21} \text{ cm}^{-2}$  given by Bohlin et al. (1978).

We consider four different torus models (discussed in Section 4) to reproduce the observed column densities. We create random lines of sight over a sphere (weighting by the angle differential area), calculating the optical depth for each random direction. This analysis is parameterized by the angle  $\phi$  defined by the angle subtended between the line of sight and the torus equatorial plane. We use a solar neighbourhood value  $R_V = 3.1$  (Schultz & Weimer 1975) to relate the Hydrogen column density  $N_H$  with the optical extinction  $A_V$ , and therefore with the optical depth  $\tau_V$  ( $A_V = 1.09\tau_V$ ),

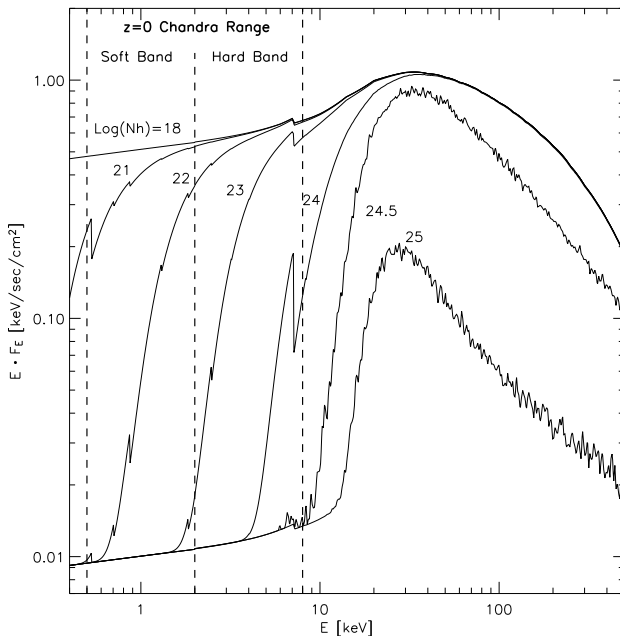


**Fig. 2.** Rest frame flux spectrum templates described in Subsection 3.1 for column densities (from left to right)  $N_H = 10^{10}, 10^{21}, 10^{22}, 10^{23}, 10^{24}$  and  $10^{25} \text{ cm}^{-2}$ , including a 2% component scattered by warm ionized material. The type 2 spectra for  $N_H > 10^{24} \text{ cm}^{-2}$  is produced by a Monte-Carlo code described by Wilman & Fabian (1999). Note that for local Compton Thick sources, the reflection component is the only emission detected by the *Chandra* band.

$$\begin{aligned}
 N_H(\phi) &= \sigma^{-1} \tau = \int \rho(r, \phi) dr \\
 &= 5.8 \cdot 10^{21} E(B - V) \text{ cm}^{-2} = 1.9 \cdot 10^{21} A_V \text{ cm}^{-2} \quad (2) \\
 &= 2.0 \cdot 10^{21} \tau_V \text{ cm}^{-2} = 2.0 \cdot 10^{21} \tau_{Vi} N_T \text{ cm}^{-2}
 \end{aligned}$$

where, if the medium is continuous,  $\rho(r, \phi)$  is the matter density distribution and  $\sigma$  the effective cross section. If the medium is clumpy,  $\tau_{Vi}$  represents the optical depth for one cloud and  $N_T$  the average number of clouds along the line of sight. It is easy to show that if the density distribution  $\rho$  has no angular dependency (i.e.  $\rho = \rho(r)$ ), then the radial dependency will be hidden by the assumed maximum column density  $N_{H\max}$  along the line of sight.

Other model parameters are also constrained by the  $N_{H\max}$  value, such as the inner radius, external radius, density in the equatorial plane, and/or cloud optical depth. In this work we fixed the maximum value for the column density at  $N_{H\max} = 10^{25} \text{ cm}^{-2}$ , according to X-Ray observations of Type II AGNs in the 0.1 – 100 keV band using the BeppoSAX X-Ray satellite by Maiolino et al. (1998), where upper limits for this value are given.

Due to the large degeneracy of the model parameters, we have chosen to use the minimum number of free parameters to describe the torus distribution. The chosen parameterizations do not describe physical sizes of the distributions explicitly,

but instead parameters such as  $R_{int}/R_{out}$  (where  $R_{out}$  is the external radius and  $R_{int}$  is the inner radius for the torus) are used. In other words, we allow our torus models depend on the inner radius, therefore on the luminosity, but keeping scale ratios (such as  $R_{out}/R_{int}$ ) fixed, hence maintaining the same shape at different scales.

As an example,  $R_{int}$  can be estimated by the “evaporation radius” for graphites (at  $T \approx 1400 \text{ K}$ ) defined by assuming thermal equilibrium between the ultraviolet incident radiation and the rate for reemission from the dust. Assuming  $a_{gr} = 0.05 \mu\text{m}$  as a typical grain size, Barvainis (1987) found that

$$R_{int} \approx 0.5 L_{UV,45}^{1/2} \text{ pc}, \quad (3)$$

where  $L_{UV,45}$  is the ultraviolet (UV) luminosity per unit of  $10^{45} \text{ erg sec}^{-1}$ . Assuming this value as a lower distance limit, we can estimate the external radius, and other model parameters, which are included in the maximum column density  $N_{H\max}$  (see Table 1).

### 3.3. Corrections for Biases

As described in the previous section, we obtain different families of synthetic column densities for each model. To compare these distributions with the observed ones, we need to correct them by including selection effects and detection biases. The sources in our sample were selected following two main criteria:

1.  $S/N > 3$  in the *Chandra* hard X-Ray band (2 – 8 keV).
2. An optical counterpart with determined spectroscopic redshift.

The X-Ray flux limit in the 2 – 8 keV band of the *Chandra* observations in the GOODS fields is  $\approx 10^{-16} \text{ erg sec}^{-1} \text{ cm}^{-2}$ . We estimate the fraction of AGNs observed by *Chandra* using the hard X-Ray luminosity function for AGNs given by Ueda et al. (2003; see Subsection 5.1 for more details), the described AGN template spectrum (Figure 2), and the GOODS flux depths versus the effective covering area from Figure 3 (based on the Alexander et al. 2003 treatment in the GOODS fields only).

Based in the X-Ray flux limits, it is found that  $< 50\%$  of the intrinsic number of Compton Thin sources ( $N_H < 10^{24} \text{ cm}^{-2}$ ) are above the flux limits of the GOODS observations. Nevertheless, the fraction of observed sources strongly depends on the integration limits used for the luminosity function. For example, considering  $0.015 < z < 5$  and  $42 < \text{Log}(L_{x2-10keV}) < 48$  as integration values, a fraction of  $\sim 50\%$  is obtained. If instead the minimum luminosity value is lowered to  $10^{41} \text{ erg sec}^{-1}$ , then only  $\sim 20\%$  is obtained. Here is clearly seen that the faint population of AGNs is very numerous. However, at this  $L_x$  level AGNs are usually confused with other types of X-Ray sources such as Ultra Luminous X-Ray Sources (ULXs) and powerful Starbursts.

To take into account the biases from the second selection criteria, we estimate the fraction of sources with spectroscopic counterparts using the data from the *Chandra* Deep Fields presented in Barger et al. (2005), Figure 1a. This estimation

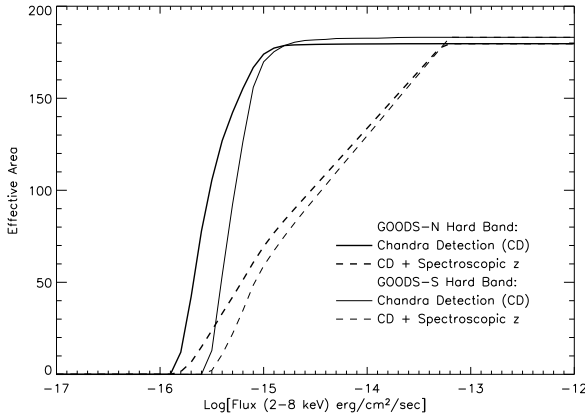


**Fig. 3.** Covering area as a function of depth as reached by *Chandra* observations in the GOODS-N ( $2\,Ms$ ,  $179.644\,arcmin^2$ ) and GOODS-S ( $1\,Ms$ ,  $183.108\,arcmin^2$ ) fields in the hard X-Ray band ( $2 - 10\,keV$ ) – based on the calculation presented by Alexander et al. (2003) over the GOODS fields only. The effective area of the spectroscopic counterparts, is also plot (based on Barger et al. 2005, Figure 1a: a straight line was assumed to describe the data points after excluding the left-most value for each CDF survey).

is mainly determined by the cut-off for viable optical spectroscopy at  $R \sim 24$ . However it does not describe the tight correlation between  $R$  magnitude and  $z$ , which reflects the difficulty of obtaining spectroscopic redshifts for Type II sources at  $z > 1$ . The spectroscopic limitation drastically modifies the number of detected sources (i.e. the effective area) depending on the detected flux. This dependency is shown in Figure 3.

Finally, using Ueda's luminosity function integrated between  $41.5 < Log(L_X\,2-10keV) < 48$  and  $0.015 < z < 5$ , and taking into account the estimation of the number of sources with available spectroscopy, we generate Figure 4 which shows the dependency of the fraction of observed sources with the column density. The figure is normalized with respect to the expected number of unabsorbed sources ( $N_H = 10^{20}cm^{-2}$ ). The estimated total fraction of observed sources is  $< 20\%$ , substantially lower than predicted before taking into account the bias introduced by the limited number of optical counterparts. Changing the luminosity function for that given by Barger et al. (2005), which describes a different evolution for Type I sources, we find almost the same results for the fraction of observed sources depending with  $N_H$  in the  $0.015 < z < 1.2$  range (less than 2% difference at  $N_H = 10^{24}cm^{-2}$  in Figure 4).

Here we see that at  $N_H \approx 10^{23}\,cm^{-2}$ , the predicted fraction of detected sources decreases by just  $\sim 10\%$  compared with unabsorbed ones, while at  $N_H \approx 10^{24}\,cm^{-2}$  it decreases by  $\sim 40\%$ . Above this value, Compton Thick sources are highly affected by flux limited detections. In this estimation we extrapolated the fraction of highly obscured AGNs, because Ueda's luminosity function does not include sources with  $N_H > 10^{24}\,cm^{-2}$ . However, this high  $N_H$  range will not be used when comparing with the observations in the GOODS fields, hence not introducing further uncertainties.

Once the corrections discussed above are introduced, synthetic histograms of Hydrogen column densities are obtained.

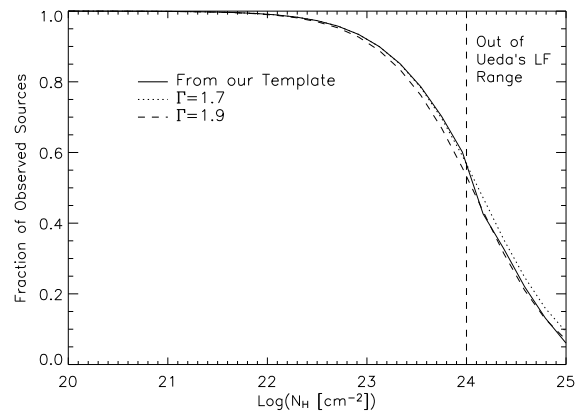


**Fig. 4.** Estimated fraction of observed AGNs depending on the Hydrogen column density along the line of sight. It is normalized with respect to the expected number ( $\lesssim 20\%$ ) of unabsorbed sources, which is integration range dependent. This plot is created using the hard X-Ray band luminosity function for AGNs given by Ueda et al. (2003), the data from Figure 3, and the assumed template from Subsection 3.1. There is also shown the estimation using simple power law models for  $\Gamma = 1.7$  and  $1.9$ . In this case, the luminosity function is extrapolated for highly obscured AGNs ( $N_H > 10^{24}\,cm^{-2}$ ), because it is not well defined in this range.

The number of simulations is the same for all the models ( $\sim 30,000$ ), ensuring smaller errors in the predicted  $N_H$  columns than those deduced from the observations. The synthetic distributions can in turn be compared with the observed values as discussed in the next section.

#### 4. Modelling the Torus

The large degeneracy of model parameters (see Section 3), and the uncertainties given by the assumptions on the population of faint sources and the determination of column densities, require us to keep the number of free parameters within our torus models to a minimum. As such, we do not allow the parameters to change with luminosity or redshift. It should be noted that Barger et al. (2005) recently presented a complete sample of local X-Ray selected AGN ( $z < 1.2$ ), in which a luminosity dependence for the fraction number of Type II over Type I AGNs is seen, as Ueda et al. (2003) proposed before. This implies a dependency of the covering factor of the dusty torus on luminosity, and therefore a change of the geometrical torus distribution. However, further confirmation of these results and an extension to higher redshifts is not available yet.

Hence, we stress that in this work we describe the AGN torus assuming different density distributions of gas and dust, given by a simple axially symmetric geometry, with no dependency on luminosity or redshift.

To find constraints over the torus model parameters which best fit the observed column densities, we use the Kolmogorov-Smirnov (KS) test and the  $\chi^2$  test, assuming poissonian error bars for small numbers (Gehrels 1986) from Figure 1. Unfortunately there are no precise estimations for the errors associated with the deduced Hydrogen column densities (see

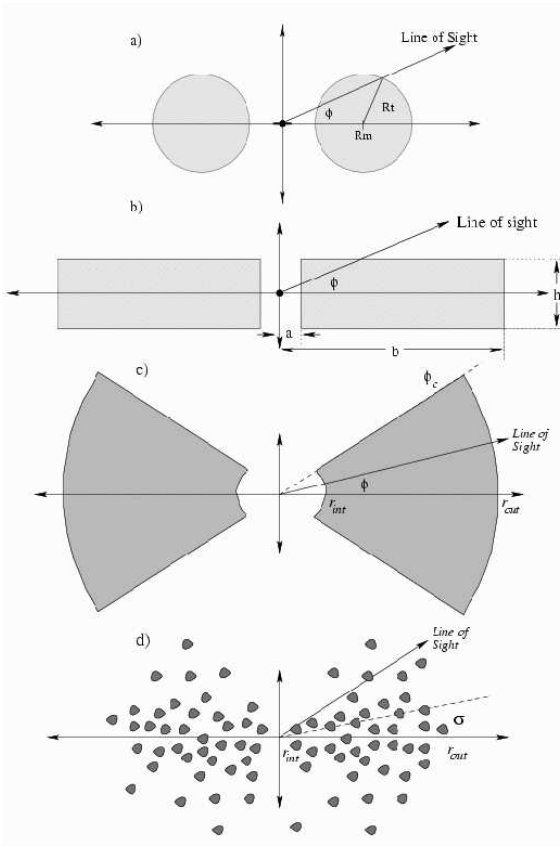


**Fig. 5.** Geometrical matter density distributions assumed for the torus models. Figures a), b) c) and d) are based following previous works by Treister et al. (2004), Pier & Krolik (1992), Granato & Danese (1994) and Nenkova et al. (2002) respectively.

Section 2.2), which might dominate over the poissonian errors. As explained before, since the *Hardness Ratio* is not sensible to the low  $N_H$  range, we generated random values for the smallest predicted column densities, to obtain a smooth accumulative distribution to be analysed using the KS test ( $\Delta N_H/N_H \approx 0.3$ ).

The following models (Figure 5) were motivated by previous works which were carried out to explain a variety of observational properties of AGNs (Treister et al. 2004; Pier & Krolik 1992, 1993; Granato & Danese 1994; Elitzur et al. 2003). A summary of the results from this section is presented in Table 1.

#### 4.1. Model 1

Following the distribution for the torus proposed by Treister et al. (2004), we modelled the geometry given by Figure 5a to find the different optical depths as a function of the line of sight,  $\phi$ . In this case the matter density is not distributed as in an homogeneous medium, but has the following dependence with  $r$  and  $\phi$ :

$$\rho(r, \phi) = \rho_{eq} \left( \frac{r_{int}}{r} \right)^\beta e^{-\gamma|\sin(\phi)|} \quad (4)$$

where  $\rho_{eq}$  is the inner density (at  $r_{int} = R_m - R_t$ ) in the equatorial plane (constrained by  $N_{Hmax}$ , see Equation 6). In this model, the free parameters are  $R_m/R_t$  (see Figure 5a),  $\gamma$ , and  $\beta$ . The analytical equations which describe the column density as a function of  $\phi$  are given by:

$$\begin{aligned} & \text{If } 0 \leq \phi < \sin^{-1}(R_t/R_m) \text{ and } \beta \neq 1 \text{ then,} \\ & N_H = N_{Hmax} e^{-\gamma|\sin(\phi)|} \times \\ & \quad \left[ \left( \cos(\phi) + \sqrt{(R_t/R_m)^2 - \sin(\phi)^2} \right)^{1-\beta} - \left( \cos(\phi) - \sqrt{(R_t/R_m)^2 - \sin(\phi)^2} \right)^{1-\beta} \right] \\ & \quad \frac{(1+R_t/R_m)^{1-\beta} - (1-R_t/R_m)^{1-\beta}}{\ln((1+R_t/R_m)/(1-R_t/R_m))} \\ & \text{If } 0 \leq \phi < \sin^{-1}(R_t/R_m) \text{ and } \beta = 1 \text{ then,} \\ & N_H = N_{Hmax} e^{-\gamma|\sin(\phi)|} \times \\ & \quad \frac{\ln \left( \left( \cos(\phi) + \sqrt{(R_t/R_m)^2 - \sin(\phi)^2} \right) / \left( \cos(\phi) - \sqrt{(R_t/R_m)^2 - \sin(\phi)^2} \right) \right)}{\ln((1+R_t/R_m)/(1-R_t/R_m))} \\ & \text{If } \sin^{-1}(R_t/R_m) \leq \phi \leq \pi/2 \text{ then, } N_H = N_{Hmin} \end{aligned} \quad (5)$$

The maximum, and minimum, column density along the line of sight is through the equatorial plane, and at the poles, respectively.

If  $\beta \neq 1$  then,

$$N_{Hmax} = \rho_{eq} r_{int}^\beta \frac{R_m^{1-\beta}}{1-\beta} \left[ \left( 1 + \frac{R_t}{R_m} \right)^{1-\beta} - \left( 1 - \frac{R_t}{R_m} \right)^{1-\beta} \right] \quad (6)$$

$$\text{If } \beta = 1 \text{ then, } N_{Hmax} = \rho_{eq} r_{int} \ln \left( \frac{1+R_t/R_m}{1-R_t/R_m} \right)$$

Using the KS and  $\chi^2$  tests to constrain the parameters which best fit the observed data, we found the results presented in Figure 6 (for  $\beta = 0.0$ ). In this case, the  $\chi^2$  test shows good agreements with the KS test (mainly over the parameter  $\gamma$ ), and both give good statistical test values.

The parameters found for  $\beta = 0.0$ , are spread between  $1.0 \leq R_m/R_t \leq 1.25$  and  $8.0 \leq \gamma \leq 11.0$ . This model gives the same results if a value  $\beta = 2.0$  is used instead. Models using  $\beta = 1.0$  and  $3.0$ , show just a small decrement for parameter  $\gamma$ , not introducing further statistical constraints. Note however, that this parameter determines those parameters hidden in Equation 6.

From the family of parameters found, we show in figure 7 some example synthetic distributions to compare with the observed column densities. Here is seen that the parameter  $R_m/R_t$  mostly affects the distribution of Type I sources, meanwhile parameter  $\gamma$  changes the fraction of Type II/I.

This model overpredicts the number of highly absorbed sources ( $N_H > 10^{23} \text{ cm}^{-2}$ ). Nevertheless as we explained in the previous sections, this population is highly affected by biases, and therefore this problem can be caused by incompletenesses in our sample.

A sketch of the geometrical distribution, choosing the best fit parameters, is given in Figure 10, where the “donut” structure of the model is clearly seen. Under these assumed parameters, an intrinsic fraction of  $\sim 23\%$  of sources have column densities  $> 10^{24} \text{ cm}^{-2}$ .

#### 4.2. Model 2

This model is proposed following previous studies by Pier & Krolik (1992, 1993) based on the IR reemission coming from the torus. We use their geometrical distribution (Figure 5b) to find the dependency of the column density with the line of sight.

This model assumes a homogeneous density and  $h/a$  and  $b/a$  as free parameters, where  $h$ ,  $b$ , and  $a$  are shown in Figure 5b. The equation which shows the dependency of the column density with the line of sight ( $0 \leq \phi \leq \pi/2$ ) is given by:

$$\begin{aligned} \text{If } 0 \leq \phi < \tan^{-1}\left(\frac{h}{2b}\right) \text{ then, } N_H &= N_{H\max} \frac{\cos(\tan^{-1}(h/2b))}{\cos(\phi)} \\ \text{If } \tan^{-1}\left(\frac{h}{2b}\right) \leq \phi < \tan^{-1}\left(\frac{h}{2a}\right) \text{ then, } N_H &= N_{H\max} \frac{\cos(\tan^{-1}(h/2b))}{b/a-1} \left(\frac{h}{2a} \sin(\phi)^{-1} - \cos(\phi)^{-1}\right) \\ \text{If } \tan^{-1}\left(\frac{h}{2a}\right) \leq \phi \leq \pi/2 \text{ then, } N_H &= N_{H\min} \end{aligned} \quad (7)$$

where the maximum column density is defined as:

$$N_{H\max} = \rho_{\text{eq}} \frac{b-a}{\cos\left(\tan^{-1}\left(\frac{h}{2b}\right)\right)} \quad (8)$$

Comparing the distribution of synthetic column densities with the observed ones, we found the results shown in Figure 6. The KS and  $\chi^2$  tests are in good agreement with each other (implying  $1.5 \lesssim h/a \lesssim 3.5$  and  $450 \lesssim b/a \lesssim 2000$ ), but the statistical values are very poor. This model shows the most extreme radial-to-vertical thickness ratio ( $b/h \approx 200 - 800$ ), even larger than for typical thin accretion disk models.

Synthetic  $N_H$  histograms are shown in Figure 7. It is seen that the parameter  $b/a$  systematically overestimates the distribution around  $N_H = 10^{22.5} \text{ cm}^{-2}$  while keeping fixed the fraction of unobscured sources. Parameter  $h/a$  changes the fraction of Type II/I, modifying also the first bin of unobscured sources.

The main problem of this model is its constant density. This means that a large geometrical structure is needed to reproduce the wide range of observed column densities (since  $N_H \propto \Delta s$ ), at the same time generating a distribution which is very sensitive to the innermost region of the torus (see Figure 10 with different axes scale).

Once the observational bias are removed, this model does not predict a large fraction of highly obscured sources, which implies that this torus model is not suitable to explain the CXRB. This model typically gives an intrinsic fraction of  $\sim 2\%$  Compton Thick sources which is basically given by a narrow angular section, near the equatorial plane, that accounts for large obscuration.

When we compare our analysis with previous results by Pier & Krolik (1992), we find large disagreements. Typical dimensions deduced by them, as restricted by IR torus reemission, are of parsec-scale, meanwhile we obtain a torus with typical scales of  $\sim 600 \text{ pc}$  assuming  $L_{UV} = 6 \cdot 10^{45} \text{ erg/sec}$ .

We conclude that this torus model can be rejected due to the numerous caveats already discussed, such as typically large outer radius, which is not seen in local AGNs (Jaffe et al. 2004;

Prieto et al 2004), the sensibility of the geometrical distribution in the inner regions, and the small number of predicted Compton Thick sources.

#### 4.3. Model 3

This model has the spatial density distribution shown in Figure 5c and is based on the work presented by Granato & Danese (1994). The density has an exponential dependency on the polar angle parameterized by a factor  $\gamma$  (when  $\phi < \phi_c$ ), and a radial power  $\beta$  dependency:

$$\rho(r, \phi) = \rho_{\text{eq}} \left(\frac{r_{\text{int}}}{r}\right)^\beta e^{-\gamma|\sin(\phi)|} \quad (9)$$

where  $\rho_{\text{eq}}$  is the inner torus density at the equatorial plane. The free parameters of the model are the opening angle  $\phi_c$ ,  $\gamma$  and  $\beta$ . The equation which describes the dependence of the column density with the line of sight is:

$$\begin{aligned} \text{If } 0 \leq \phi < \phi_c \text{ then, } N_H &= N_{H\max} e^{-\gamma|\sin(\phi)|} \\ \text{If } \phi_c \leq \phi \leq \pi/2 \text{ then, } N_H &= N_{H\min} \end{aligned} \quad (10)$$

where  $N_{H\min}$  and  $N_{H\max}$  are fixed parameters at  $10^{20}$  and  $10^{25} \text{ cm}^{-2}$  respectively. The minimum value fixes  $N_H$  at the poles and the maximum value fixes  $N_H$  at the equatorial plane.

$$\begin{aligned} \text{If } \beta \neq 1 \text{ then, } N_{H\max} &= \rho_{\text{eq}} r_{\text{int}}^\beta \left(\frac{r_{\text{out}}^{1-\beta} - r_{\text{int}}^{1-\beta}}{1-\beta}\right) \\ \text{If } \beta = 1 \text{ then, } N_{H\max} &= \rho_{\text{eq}} r_{\text{int}} \ln\left(\frac{r_{\text{out}}}{r_{\text{int}}}\right) \end{aligned} \quad (11)$$

Searching for best fit parameters using KS and  $\chi^2$  tests, we obtain the results shown in Figure 6. This model gives very good statistical values ( $P_{KS} \approx 0.6$  and  $\chi^2_{\nu, \min} = 0.88$ ), obtaining also an overlap, in both axes, of the parameters found by each test. Parameters between  $51.6^\circ = 0.9 \lesssim \phi_c \lesssim 1.2 = 68.8^\circ$  and  $9.3 \lesssim \gamma \lesssim 11.5$  are found.

The sharp gap seen at  $N_H \lesssim 10^{21} \text{ cm}^{-2}$  corresponds to the transition produced when the line of sight no longer hits the torus ( $\phi > \phi_c$ ). Simulations are shown in Figure 7. Changes in the value of  $\phi_c$  affect the distribution over Type I sources only, while parameter  $\gamma$  affects the number of sources at  $N_H \approx 10^{21} \text{ cm}^{-2}$  and changes the fraction of Type II/I. This model, being very simple, can describe the wide range of observed column densities thanks to the exponential angle dependency (see Figure 10). The estimated intrinsic fraction of Compton Thick sources is  $\sim 23\%$ .

When we compare our results with the previous work by Granato & Danese (1994), we find that our analysis can clearly constrain the  $\phi_c$  parameter, although for larger  $\gamma$  values it is not well constrained. Granato & Danese found that the spectral energy distribution for the reemission does not depend strongly on this parameter. On the other hand, we can not constrain the outer radius, since this scale parameter is contained in  $N_{H\max}$  (Equation 11), and it could be easily adjusted to any value (e.g.  $> 100 \text{ pc}$  scale found by Granato & Danese 1994).

Model	$P(KS)_{max}$	$\chi^2_{y,min}$	Parameter 1	Parameter 2	Parameter 3	$R_{out}[pc]$	$\rho_{eq}[cm^{-3}]$
1	$\sim 0.4$	1.16	$1.0 \lesssim R_m/R_i \lesssim 1.25$	$8.0 \lesssim \gamma \lesssim 11.0$	$0.0 \lesssim \beta \lesssim 4.0^{\ddagger}$	$> 10.8$	$> 3.4 \cdot 10^5^{\dagger}$
2	$\sim 0.06$	2.48	$1.5 \lesssim h/a \lesssim 3.5$	$450 \lesssim b/a \lesssim 2000$	X	$540 - 2400$	$1.6 - 7.2 \cdot 10^3$
3	$\sim 0.6$	0.88	$0.9 \lesssim \phi_c [rad] \lesssim 1.2$	$9.3 \lesssim \gamma \lesssim 11.5$	X	$10.0^*$	$3.7 \cdot 10^5^{\dagger}$
4	$\sim 0.015$	3.11	$0.34 \lesssim \sigma [rad] \lesssim 0.41$	$\tau_{Vi} \lesssim 1.0$	X	-	-

Notes . -

\* indicate a fixed parameter.

$\dagger$  these parameters can be modified taking into account radial dependencies for the model.

$\ddagger$  obtained assuming  $\gamma = 9.5$ .

**Table 1.** Summary for the estimated range of parameters, using the analysis explained in Section 4 (ranges are deduced from KS &  $\chi^2$  contour plots of Figure 6). Last two columns are deduced considering a UV luminosity for the source of  $6 \cdot 10^{45} erg sec^{-1}$  in Equation 3. No radial dependencies for the density distribution ( $\beta = 0.0$ ) are assumed in the models. In Model 3 we use a fixed parameter  $R_{out} = 10 pc$  to estimate a density at the equatorial plane. Last columns have not been included here for Model 4 due to the different cloud treatment as explained in Subsection 4.4.

#### 4.4. Model 4

Many previous theoretical models trying to reproduce the IR reemission coming from the obscuring torus were based on continuous density distributions (as those presented in Models 1 to 3). Elitzur et al. (2003) have developed the formalism to handle dust clumpiness and their results indicate that the inclusion of thick clouds may resolve the difficulties encountered by previous theoretical efforts trying to reproduce the observed IR SED of local AGNs. They had shown that the problems are naturally resolved if a clumpy media formed by  $\sim 5 - 10$  clouds along radial rays (each one with  $\tau_{Vi} \gtrsim 40$ ) through the torus is considered. The fundamental difference between clumpy and continuous density distributions is that radiation can propagate freely between different regions of an optically thick medium when it is clumpy, but not otherwise.

Following Elitzur et al. (2003) we define the model given by Figure 5d, considering a spatially random density cloud distribution per length unit given by:

$$n_T(r, \phi) = n_{eq} \left( \frac{r_{int}}{r} \right)^\beta e^{-\phi^2/\sigma^2} \quad (12)$$

where  $n_{eq}$  is the inner number of clouds by length unit in the equatorial plane,  $\sigma$  the half opening angle for the angular distribution, and  $\beta$  a power radial dependency. Integrating the last equation along the line of sight, we obtain the average number of clouds,  $N_T$ , as a function of the line of sight, parameterized by the angle  $\phi$ :

$$N_T(\phi) = N_{eq} e^{-\phi^2/\sigma^2} \quad (13)$$

where  $N_{eq}$  is the average number of clouds along the equatorial plane:

$$\begin{aligned} \text{If } \beta \neq 1 \text{ then, } N_{eq} &= n_{eq} \frac{r_{int}^\beta}{1 - \beta} (r_{out}^{1-\beta} - r_{int}^{1-\beta}) \\ \text{If } \beta = 1 \text{ then, } N_{eq} &= n_{eq} r_{int} \ln \left( \frac{r_{out}}{r_{int}} \right) \end{aligned} \quad (14)$$

Assuming  $\tau_V = N_T \tau_{Vi}$ , and using a standard gas to dust ratio (Bohlin et al. 1978), we can estimate the Hydrogen column density dependency on the line of sight, as:

$$N_H(\phi) = N_{Hmax} e^{-\phi^2/\sigma^2} \quad (15)$$

The fixed parameter  $N_{Hmax}$  constrains the optical depth, the number of clouds along the line of sight at the equatorial plane, and the parameter  $\beta$ :

$$N_{Hmax} = 2.0 \cdot 10^{21} N_{eq} \tau_{Vi} \quad (16)$$

The only free parameter for the angular distribution is given by  $\sigma$ . Restricting  $N_T$  to discrete clouds and assuming poissonian probabilities for the clumps in the line of sight, it is also possible to constraint the optical depth per cloud,  $\tau_{Vi}$ . In the case when the optical depth per cloud tend to zero but  $N_T$  tend to infinity, the continuous case is obtained again, where column densities are allowed to have any value. Note that  $N_T = 1$  and  $\tau_{Vi} = 40$  (minimum value per cloud determined by Nenkova et al. 2002) imply a minimum column density of  $8.0 \cdot 10^{22} cm^{-2}$ , becoming impossible to obtain smaller values for the predicted column densities. Clearly, smaller optical depths per cloud are necessary to explain the observed distribution of  $N_H$  values. However, absorption given by overdensities of diffuse material located in the outer regions of the torus could be responsible of these small observed column densities.

The statistical tests to find the best-fit values are shown in Figure 6, where both tests show good correlations. To avoid numerical anomalies given by the discrete analysis, the  $\chi^2$  test is computed over the averaged distribution obtained using different bins of  $N_H$ . However, multiple minima in the  $\chi^2$  distribution are found. Values between  $19.5^\circ = 0.34 \lesssim \sigma \lesssim 0.41 = 23.5^\circ$  and  $\tau_{Vi} \lesssim 1.0$  are preferred, although with poor statistical values. Clear discrepancies are seen when we compare the synthetic and the observed column densities in Figure 7. The parameter  $\sigma$  changes the number of objects at  $N_H = 10^{20} cm^{-2}$  and at  $N_H = 10^{25} cm^{-2}$ , without altering significantly the middle values. On the other hand, the discretization of the obscuring torus into discrete clouds creates a dichotomy between Type II and Type I objects, where the minimum value of  $N_H$  is given by the optical depth of a single cloud. This free parameter does not introduce changes in the shape of the distribution of column densities with intermediate values either.

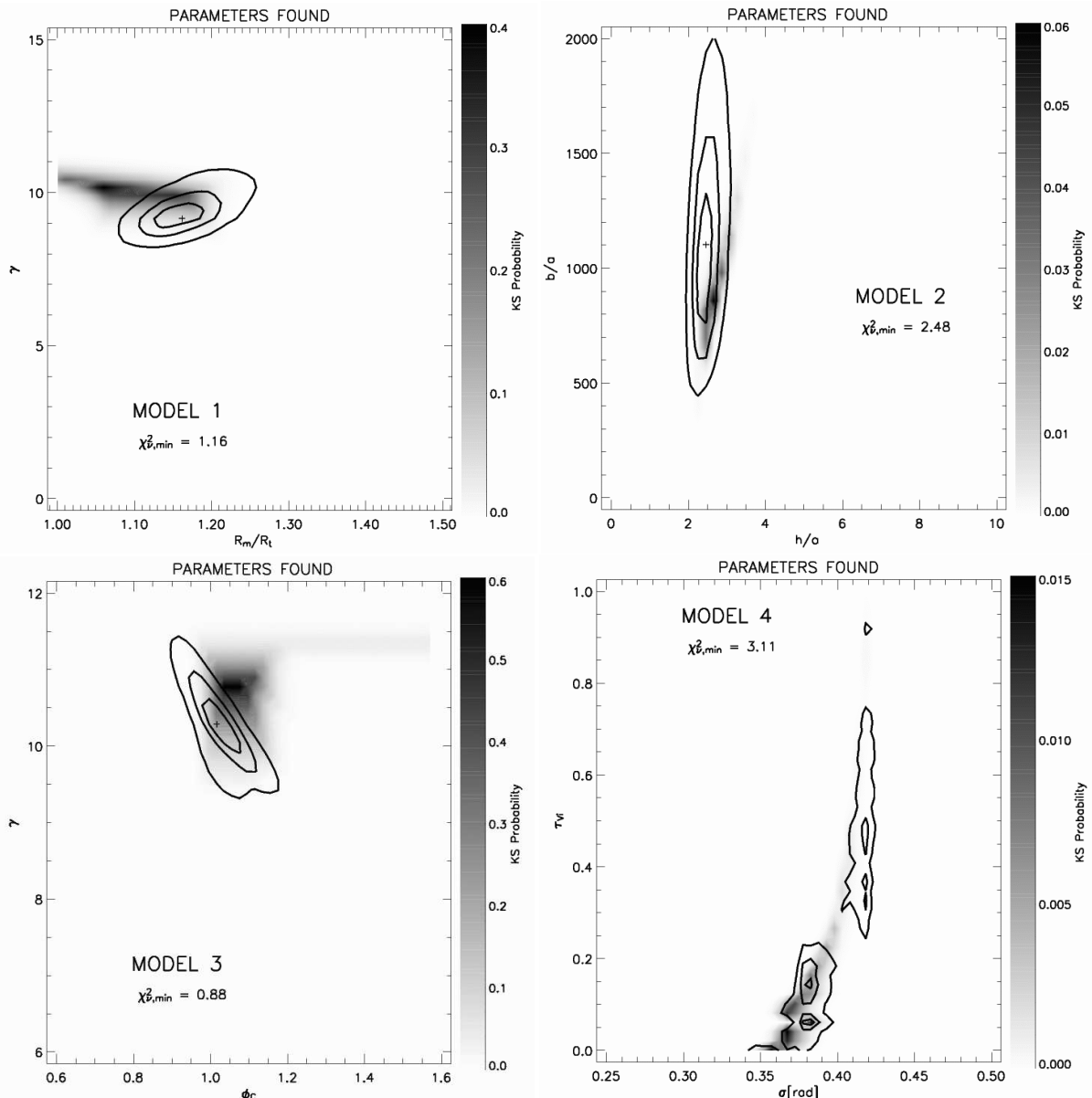


**Fig. 6.** Parameters found for each model following Section 4. Contour plot shows the KS test between the observed cumulative distribution and that predicted by our models. Black colour represents the highest probability values and white the lowest ones. Overplotted are the results from the  $\chi^2$  tests. The black contours represent 1, 2 and 3  $\sigma$  values from the best fit parameter. Note that for Model 1  $\beta = 0.0$ .

We conclude, that this model cannot generate the observed  $N_H$  distribution. From Figure 10 it is clear that this model overestimates the number of Compton Thick sources near the equatorial plane (giving an intrinsic fraction of  $\sim 37\%$ ), being impossible to generate the observed distribution of column densities. This even applies after trying different values of  $N_{H\max}$ .

When we compare our parameters with the results coming from the reemission treatment given by Elitzur et al. (2003), we found that our typical Gaussian angular distributions are smaller than Elitzur's values. In fact, they find a valid range of  $\sigma = 45^\circ \pm 15^\circ$ , larger than  $\sim 20^\circ$ . Their estimations for the number of coulds along the equatorial plane ( $N_{\text{eq}} \approx 5 - 10$ ) correspond to a maximum column density of  $\sim 10^{24} \text{ cm}^{-2}$  (see

Equation 2), one order of magnitude smaller than our assumptions. In our models, since  $N_{H\max} = 10^{25} \text{ cm}^{-2}$ , the value of  $N_{\text{eq}}$  depends on the assumed  $\tau_{Vi}$ .

Note that  $N_H \propto N_T$ , then this clumpy model requires a wide range for the average number of clumps (at least  $\sim 3$  orders of magnitude) to describe the wide range of observed  $N_H$ s.

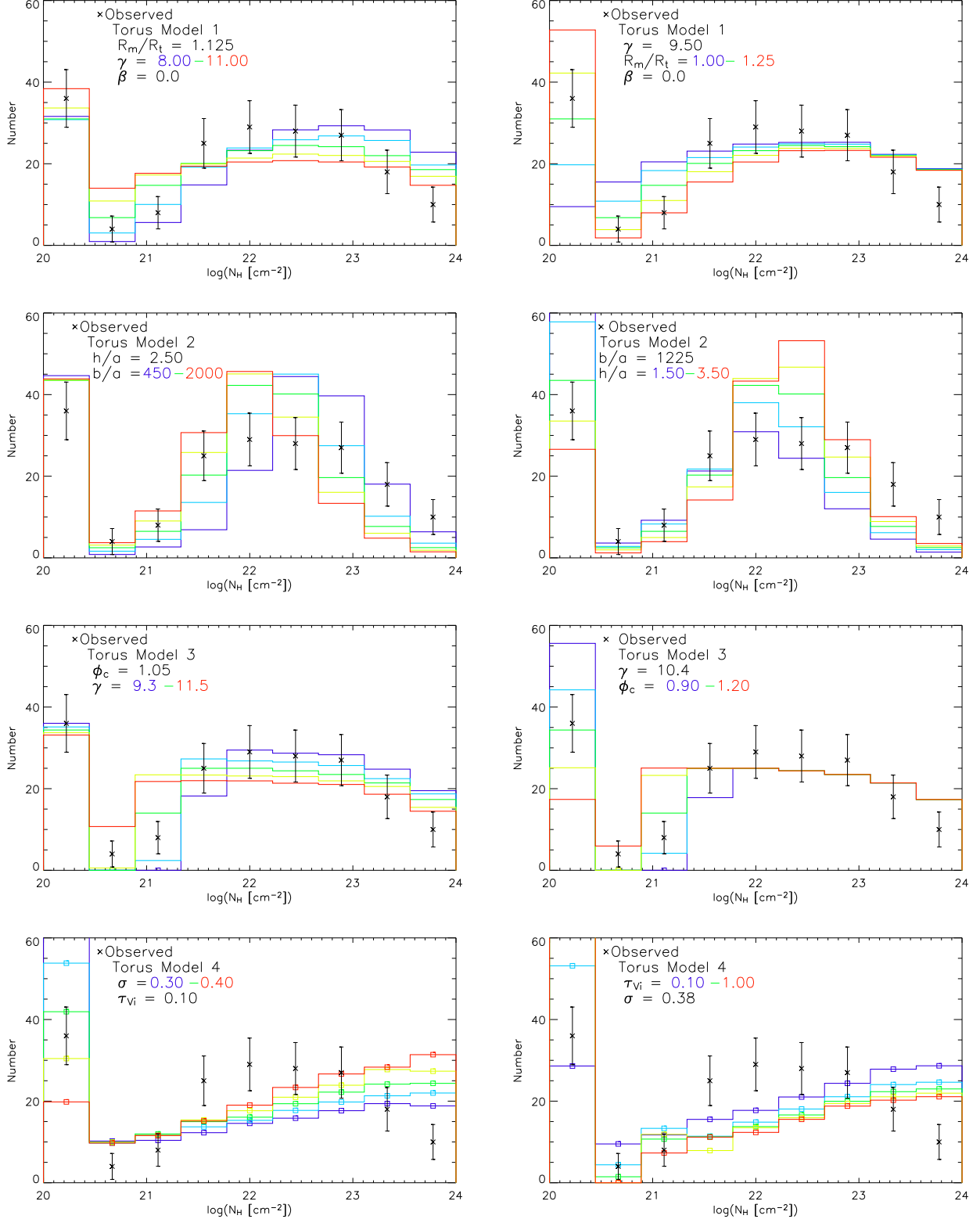


**Fig. 7.** Comparison between the column densities for the observed *Chandra* sources in the GOODS fields (crosses) and the best fit results obtained from our simulations, as predicted by the KS and  $\chi^2$  tests. Models are corrected for biases using data from Figure 4. For each model, the histograms represent the range of interest of one parameter only.

## 5. AGNs and the Cosmic X Ray Background

Several pieces of evidence have demonstrated that the bulk of the Cosmic X-Ray Background (CXR) above the energy of  $\sim 2 \text{ keV}$  is extragalactic in origin (Fabian & Barcons 1992). Actually, for a long time it had been predicted that the CXR is made up from the integration of AGNs over the cosmic time (Setti & Woltjer 1989).

This scheme has been confirmed by deep X ray surveys, starting from the early observations with the X ray satellites GINGA and ROSAT (Fabian & Barcons 1992) to the deep surveys made by the space telescopes *Chandra* (Moretti et al. 2003) and XMM-*Newton* (Hasinger et al. 2001). Recent CXR estimations, based in the *Chandra* Deep Fields, give resolved fractions of  $77\% \pm 3\%$  and  $79\% \pm 8\%$  for the  $1 - 2 \text{ keV}$  and  $2 - 8 \text{ keV}$  energy ranges respectively (Hickox & Markevitch 2005), where AGN make the 83% and the 95% of the resolved fractions in the soft and hard band respectively.

We use this picture to find possible constraints to our torus models.

### 5.1. The Luminosity Function

Using a compilation of *ASCA*, *HEAO* – 1 and *Chandra* observations, Ueda et al. (2003) constructed a luminosity function for AGNs (247 sources) in the hard X ray band ( $2 - 10 \text{ keV}$ ). Ueda's luminosity function shows a luminosity dependent density evolution, in which the low luminosity AGN population peaks at a lower redshift than the high luminosity sources. This is consistent with optical quasar observations in which this population peaks at redshift  $\sim 2$  (Boyle et al. 2000).

The main impact of Ueda's work is that by using hard band detections only, it gives the best estimation of the number of AGN in the Universe (Mushotzky 2004) avoiding a possible contamination from thermal sources (such as diffuse Galactic and/or Solar system emission, intergalactic warm gas and Star-burst galaxies). However, as most surveys, this luminosity function is biased against low luminosity sources, due to either, low intrinsic power or large amounts of absorption (up to 4 orders of magnitude larger in Type II than in Type I AGNs in the  $2 - 10 \text{ keV}$  rest-frame band). In fact, the demographics of the low luminosity and the highly obscured AGN populations remains unclear.

Ueda's luminosity function is defined only for AGNs in the  $10^{41.5} - 10^{46.5} \text{ erg sec}^{-1}$  luminosity range in the  $2 - 10 \text{ keV}$  energy range, up to  $z \approx 3$ , and in the  $20 < \text{Log}(N_H \text{ cm}^{-2}) < 24$  range, implying that our work needs an extrapolation to extract information for column densities above  $10^{24} \text{ cm}^{-2}$  (i.e. for Compton Thick sources).

### 5.2. Calculating the Cosmic X-Ray Background

The number of AGNs per unit redshift, per unit luminosity and per unit solid angle, is given by:

$$\frac{dN(L_X, z)}{d\text{Log}(L_X) dz d\Omega} = \frac{d\Phi(L_X, z)}{d\text{Log}(L_X) dz d\Omega} \frac{dV_{co}(z)}{d\Omega} \quad (17)$$

where the first term in the right hand-side of the equation is the luminosity function and the second term is the differential comoving cosmological volume, which weights the probability to find a source at a certain redshift given the Universe geometry.

We introduce our models, described in Section 4, by weighting the number of sources per bin of  $N_H$  as predicted before. The total AGN contribution to the CXR is given by the integration over luminosity and redshift (Ueda et al. 2003).

$$\begin{aligned} F_E^{\text{XRB}} &= \frac{dF^{\text{XRB}}}{d\Omega dE} \\ &= \int_{z_{\min}}^{z_{\max}} \int_{\text{Log}(L_X)_{\min}}^{\text{Log}(L_X)_{\max}} \sum_{N_{Hi}=N_{H\min}}^{N_{H\max}} f(N_{Hi}) \times \\ &\quad \frac{dN(L_X, z)}{d\text{Log}(L_X) dz} \frac{dF}{dE}(L_X, z, N_{Hi}, \Gamma) d\text{Log}(L_X) dz \end{aligned} \quad (18)$$

where  $\frac{dF}{dE}$  is given by the assumed AGN template (Equation 1), and  $f(N_{Hi})$  is the normalized distribution of column densities as predicted by our torus models, well defined in the  $20 < \text{Log}(N_H \text{ cm}^{-2}) < 24$  range according to Ueda's luminosity function. Hence,

$$\sum_{N_{Hi}=10^{20} \text{ cm}^{-2}}^{10^{24} \text{ cm}^{-2}} f(N_{Hi}) = 1 \quad (19)$$

Ueda's luminosity function predicts a different AGN evolution for different luminosities, a process that must be related to the nuclear activity, and therefore to the dynamics of inflowing material in the circumnuclear region, and very likely, to the torus. Also, there is now some evidence that the fraction of Type II to Type I depends also on luminosity (Ueda et al. 2003, Barger et al. 2005), which could be understood as a smaller torus filling factor in the high luminosity sources due to higher radiation pressure. In Figure 8 we estimated how large a change the assumption of Barger's luminosity function (for all and Type I AGNs) instead of the Ueda's, would make to the contribution to the CXR. This Figure shows that the fractional difference between the two different luminosity functions (assuming the AGN emission template and a particular  $N_H$  distribution) is quite flat in the range of interest (Hard X-Ray band), therefore easily explained by the uncertainties in the normalization factor of the background emission. We conclude that introducing a luminosity dependency as proposed by Barger et al. (2005) does not change significantly the synthetic CXR (see also Treister et al. 2005).

### 5.3. Spectral Index in the 2-10 keV Band

From previous studies (Comastri et al. 1995; Ueda et al. 2003), it is known that the contribution from unabsorbed sources is mostly seen in the soft part of the CXR ( $\lesssim 5 \text{ keV}$ ), while at high energies the flux is essentially dominated by the contribution from Type II sources. This implies that the spectral index in the  $2 - 10 \text{ keV}$  band is harder when the Type II/I fraction increases, and softer when it decreases. Hence, since the flux

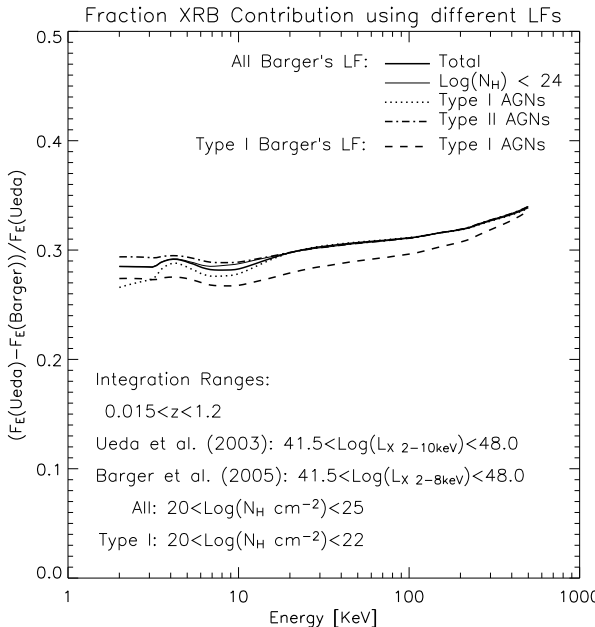


**Fig. 8.** Fraction flux contribution to the CXRB using different luminosity functions and the  $N_H$  distribution given by Model 1 ( $R_m/R_t = 1.1$ ,  $\gamma = 10.0$ ) and  $\beta = 0.0$  (see Subsection 5.2). Here Ueda et al. (2003) LDDE is compared against the low redshift hard X-Ray luminosity function (all sample and Type I only) given by Barger et al. (2005). The comparison uses the  $0.015 < z < 1.2$  range, where both luminosity functions are well defined, but extrapolating for highly absorbed sources ( $N_H > 10^{24} \text{ cm}^{-2}$ ) in the thick solid line. Note that the flat dependency below 10 keV does not introduce further discrepancies in the CXRB prediction, because the value  $\sim 0.3$  is within the observational uncertainties of the CXRB normalization.

contribution from these two populations is similar in the band of interest, this index ( $\Gamma_{2-10\text{keV}}^{\text{CXR}} \approx 1.4$ ) might give a reliable constraint for the torus parameters. Also, since the index can be observationally determined from the data obtained with the *HEAO* – 1 satellite only, it is not affected by the well known uncertainties from joining together the spectra obtained from more than one mission.

To compare results between this spectral index indicator and the column density analysis (Section 4), torus parameters were selected inside 1, 3 and  $5\sigma$ , according to the  $\chi^2$  test of the synthetic versus observed CXRB spectral slope in the 2 – 10 keV band. A normalization factor (typically of  $\sim 1.2$  at 10 keV) is used to match the observational CXRB with our synthetic predictions, in good agreements with the observational uncertainties (De Luca & Molendi 2004)

Results for each model are presented in Figure 9. Typical values of  $b/h \approx 100$  and  $\sigma \approx 0.33 \text{ [rad]} \approx 19^\circ$  are found in Models 2 and 4, but without an overlap between this analysis and the results found in Section 4. On the other hand, Model 1 and 3 show very good correlations. Parameter  $\gamma$  was again constrained between  $9.0 \lesssim \gamma \lesssim 11.0$  for each model, although parameters  $R_m/R_t$  and  $\phi_c$  were not constrained. It is interesting to note that the models with the best statistical results from the

$N_H$  analysis, (1 and 3, see Table 1) are also those which match best the spectral CXRB index.

As mentioned before, the spectral index (2 – 10 keV) is a good indicator of the Type II/I fraction of each model. This dependency is clearly seen in parameters such as  $R_m/R_t$  and  $\phi_c$ , which are not constrained by this analysis because they do not change the Type fraction (see Figure 6).

The main caveat of this analysis comes from the uncertainties in the normalization factor of the CXRB, which lets the possibility that a large number of faint Type II sources can be adjusted in the fit. This problem is seen in the predicted intrinsic Type II/I fraction value (i.e. not corrected by selection biases, and including  $N_H > 10^{24} \text{ cm}^{-2}$  AGNs), where a fraction as high as  $\sim 6$  is found for Model 2, being just  $\sim 2$  in the remaining models.

As can be seen in Figure 11, where we used the models' best fit parameters to compute the CXRB, none of our models can reproduce the observed hump at  $\sim 30 \text{ keV}$  (thick solid line). Observed sources with  $N_H < 10^{24} \text{ cm}^{-2}$  already show that their fractional contribution to the CXRB significantly decreases with increasing energy (Worsley et al. 2005). The inclusion of highly absorbed sources ( $N_H > 10^{24} \text{ cm}^{-2}$ ) as predicted by the torus models, solves this problem at  $< 20 \text{ keV}$ . However at higher energies a flux excess is still observed. The inclusion of a population of Compton Thick sources ( $N_H = 10^{25} \text{ cm}^{-2}$ ) at  $z \approx 0$  gives an adequate fit to the CXRB. These sources were supposed to have intrinsic X-Ray luminosities of  $L_X \approx 10^{41.5} \text{ erg sec}^{-1}$  uniformly distributed over  $0.015 < z < 0.2$ , and doubling the total AGN number estimated by Ueda's luminosity function in that range. This population has a theoretical density distribution of 33 sources/deg $^2$ , but might be completely missed in the deep surveys, such as GOODS, since it cannot be detected in the hard energy bands of *Chandra* or *XMM-Newton*.

Nevertheless, the excess of flux at higher energies can also be explained by assuming different absorption properties, for example sources with higher metallicity (see Treister & Urry 2005), which generates harder photoelectric absorptions and then a CXRB spectral shift to higher energies (Wilman & Fabian 1999).

Since the CXRB emission at high energies ( $> 20 \text{ keV}$ ) comes mainly from photons which are subject to reprocessing and power-law cut-off, the photoelectric absorption (in the local frame at  $\lesssim 10 \text{ keV}$ ) given by the torus do not modify this high CXRB energy range. At energies  $\sim 100 \text{ keV}$ , it is possible to lift the synthetic spectrum assuming just a higher value for  $E_C > 300 \text{ keV}$ , not introducing further discrepancies for the spectral index in the 2 – 10 keV range. Above energies  $> 100 \text{ keV}$  a non-thermal component (presumably from “Blazars”) with much higher cut-off energy values  $\sim 1 \text{ MeV}$  is necessary to reproduce the CXRB emission (Ueda et al. 2003).

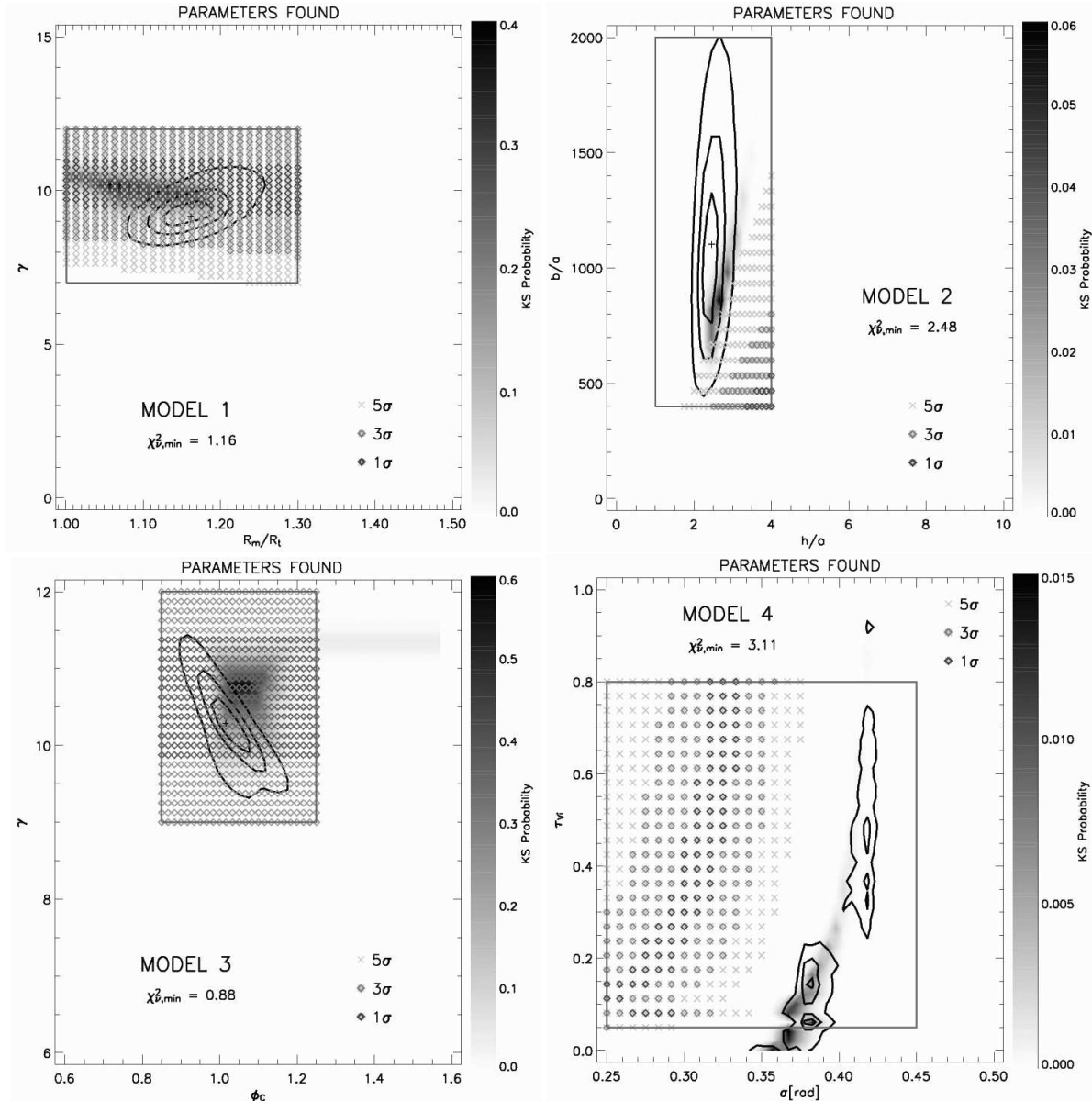


**Fig. 9.** Comparison between the results obtained from the column density analysis (Figure 7), and the parameters constrained by the CXRB spectral index analysis. These are obtained using the  $\chi^2$  test between the desired spectral index ( $\Gamma_{2-10\text{keV}}^{\text{CXRb}} \approx 1.4$ ) and the synthetic ones (at 1, 3, and 5  $\sigma$ ), using error bars following Gruber et al. (1999).

## 6. Discussion

### 6.1. The Unification Model

The work of Barger et al. (2005), based on a complete AGN sample for  $z < 1.2$ , shows a dependency of the fraction Type II/I with luminosity. This observational evidence implies that our simple *Unification Model*, where the torus does not evolve with neither luminosity nor redshift, might not be an accurate representation. In this work, the Ueda's luminosity function is directly used to estimate the observed AGN fraction dependency on the column density (Figure 4) and to integrate the flux contribution to the CXRB (Figure 8). In both cases, using instead Barger's luminosity function, we found a negligible change for these estimations, and therefore our torus model results are not particularly sensitive to a swap between

these two luminosity functions. Treister & Urry (2005) found a simple explanation for Barger's results assuming a *Modified Unification Model*, where the percentage of obscured AGNs varies linearly from 100% at  $L_X = 10^{42} \text{ erg sec}^{-1}$  to 0% at  $L_X = 3 \cdot 10^{46} \text{ erg sec}^{-1}$ , therefore, that study implies the evolution of the torus parameters. However, the present statistics in the distribution of column densities from GOODS does not allow us to constrain more free parameters to test for a luminosity evolution. In this context, our results can be regarded as a luminosity average of the distribution of the covering factor.

The *Unification Model* (simple or/and modified) also over-predicts the number of the so-called “obscured quasars” which are not observed. Results in the search for Type II QSOs from the Sloan Digital Sky Survey show around 300 objects spectroscopically classified as narrow-line AGNs in the  $0.3 < z < 3$

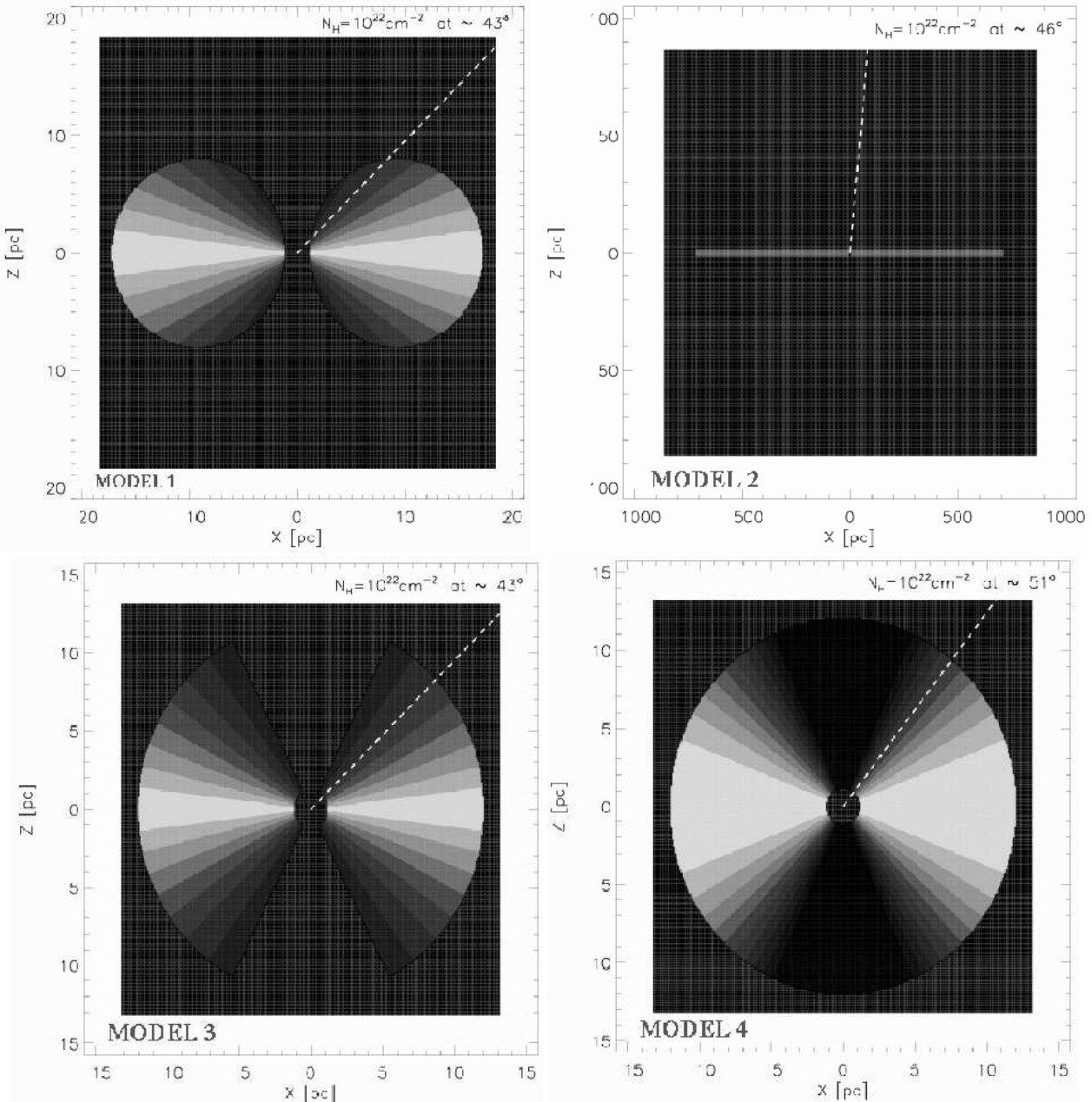


**Fig. 10.** Geometrical matter density distribution using best fit parameters for each model. Model 1:  $R_m/R_t = 1.15$ ,  $\gamma = 10.0$  and  $\beta = 0.0$ ; Model 2:  $h/a = 3.0$  and  $b/a = 600$ ; Model 3:  $\phi_c = 1.1$  and  $\gamma = 10.0$ ; Model 4:  $\sigma = 0.34$  and  $\tau_{Vi} \ll 1$  (continuous case). The inner radius is set at  $1.2\text{pc}$  for all models, and an outer radius at  $12\text{pc}$  for models 3 and 4 (but adjustable for more compact structures). Different shades mean  $\Delta \log(N_H) = 0.5$ , starting from  $10^{25} \text{ cm}^{-2}$  at the equatorial plane. The dashed line represent the line of sight that divides the Type I and the Type II sources. Note that Model 2 is shown at a different scale.

redshift range (Zakamska et al. 2002), this number being only 0.6% of the total AGN population in the SDSS for  $z > 0.3$ . This problem is probably due to the bias introduced by optical spectroscopic counterparts which has a limit for reliable redshift determinations at  $R \sim 24$ , generating a cut-off at around  $z \sim 1$  to the tight relationship between  $R$  and  $z$  for Type II sources (see Figure 6 in Barger et al. 2005). Note that the observed number of hard X-Ray sources detected by Chandra in the GOODS fields is 351, but only 185 have a reliable optical

counterpart with determined spectroscopic redshift (Treister et al. 2004).

Despite these problems, evidence for the *Unification Model* is supported by a large variety of observational properties in low redshift AGN. For example, polarized emission from Type II objects (Antonucci 1993), spatial anisotropies in the extended radio structures (Falcke et al. 1998), photoelectric absorption and reprocessed emission in X-Rays (Lightman & Rybicki 1980), the detection of broad emission lines at IR wavelengths in Type II sources (Ruiz et al. 1994), and IR emis-

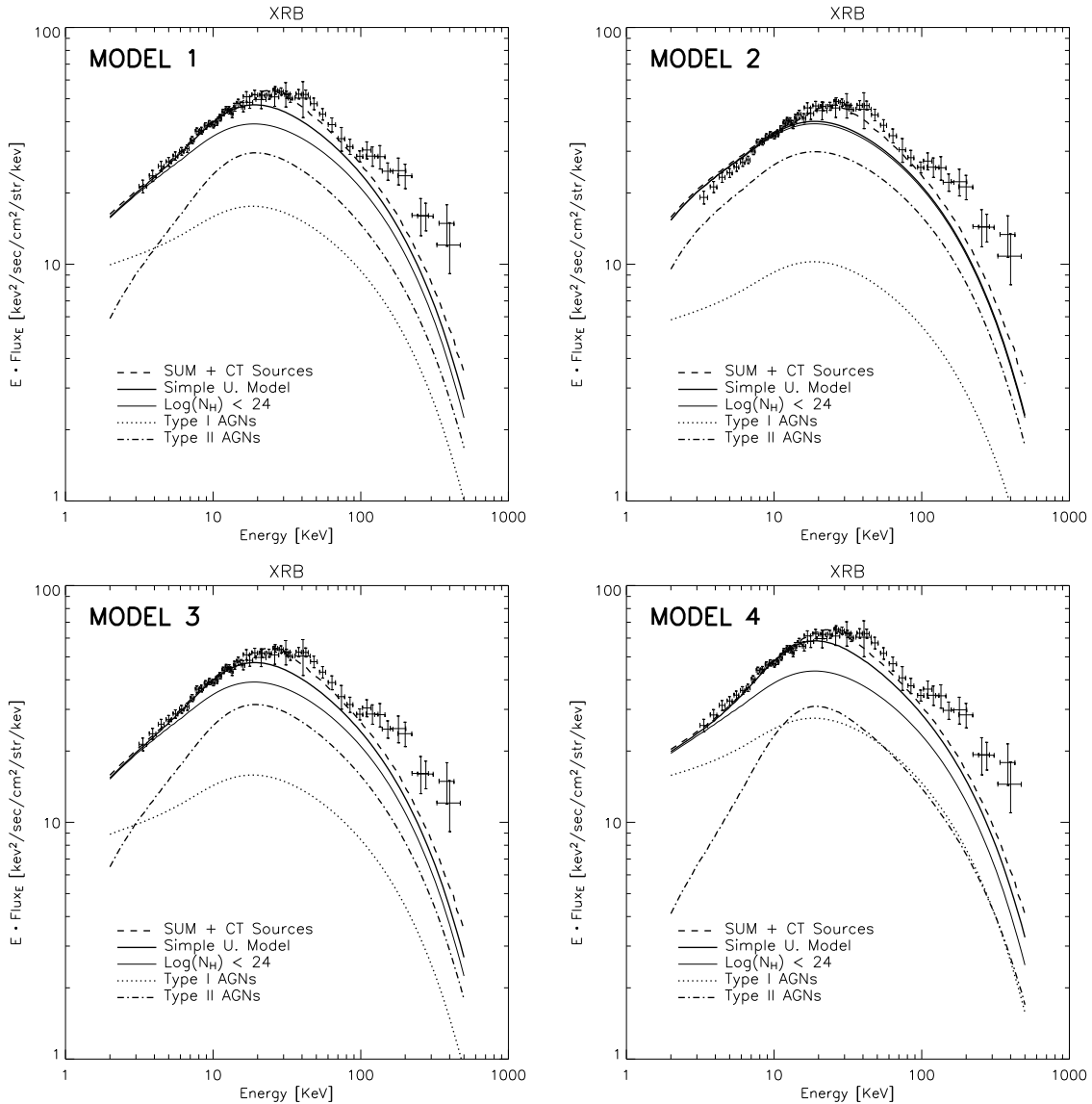


**Fig. 11.** Spectral CXRB predictions (thick solid line) using parameters selected from the overlapping of the results from the observed GOODS  $N_H$  distribution and the spectral CXRB slope in the  $2 - 10$  keV range. Parameters - Model 1:  $R_m/R_t = 1.1$ ,  $\gamma = 10.0$  and  $\beta = 0.0$ ; Model 2:  $h/a = 3.0$  and  $b/a = 500$ ; Model 3:  $\phi_c = 1.1$  and  $\gamma = 10.0$ ; Model 4:  $\sigma = 0.3$  and  $\tau_{Vi} = 0.3$ . The solid thin black line represents the contribution from Compton Thin AGN, while the dotted and dot-dashed lines are the contributions from Type I and Type II sources (not including the added Compton Thick sources), respectively. The thick dashed line represents the modified results by adding a contribution from local Compton Thick sources ( $N_H = 10^{25} \text{ cm}^{-2}$ ) to the predicted thick solid line. This population represents  $\sim 1 - 2$  times the local AGN population ( $0.015 < z < 0.2$ ). Observational data are obtained from Gruber et al. (1999) and are normalized by a factor 1.2 at 10 keV in each model, in agreement with CXRB uncertainties.

sion excess (Nenkova et al. 2002). At high- $z$ , the most clear evidence for the presence of obscured sources, as we have seen, is the hard nature of the CXRB.

## 6.2. Derived Column Densities

From measuring column densities, it is not possible to determine how far from the central source the absorption is produced. This implies that clumps located closer than the graphite sublimation radius will not follow the local *Gas to Dust* ratio.

This scenario is supported by the variability to the observed column densities (Risaliti et al. 2005). This effect can change the  $N_H$  distribution in favor of large column densities. The assumption of different media properties, such as different metallicities, gives a harder photoelectric absorption also increasing the estimate in the number of Type II sources. It is not possible at this point to clarify these issues. Also, changing the parameter  $R_V$  from 3.1 to 5.0 produces a small and negligible difference in our results.

However, the largest assumption in our treatment comes from the AGN template. Differences in the adopted reflection and the scattering reprocessed component can largely change the estimated column density derived from the Hardness Ratio. This assumption mainly affects the high redshift regime, and the highly absorbed low redshift sources, resulting in low column densities.

### 6.3. Torus Model Results

Recent IR observations have derived compact torus structures in near Seyfert II galaxies (Jaffe et al. 2004; Prieto et al. 2004, 2005; Swain et al. 2003) in agreement with typical sizes predicted from model 3 and 4.

Nowadays, it is well known that a constant torus density distribution does not explain the reemission IR spectrum, but the inclusion of clumps solve these problems. Models, 1 to 3, can be discretized using Equation 2, and considering small optical depths per cloud to allow predictions of Type I sources at  $\sim 10^{21} \text{ cm}^{-2}$ , avoiding a large dichotomy between Type II and Type I objects.

Exponential angular dependencies of the parameter  $\rho$  (see Equation 2) allow density decrements, from the equatorial plane to the poles, so that a wide range of  $N_H$  can be obtained, implying that Model 1 and 3 are the most favorable obscuring structures. On the other hand, radial dependencies for the models ( $\beta \neq 0$ ) can shrink the effective torus radius, increasing the inner equatorial density, more according with dynamical constraints of the thick clumpy torus (see Beckert & Duschl 2004).

To obtain better constraints for torus models based on the observed column densities, X-ray spectroscopy for AGN at moderate and high  $z$ , not only band fluxes (to derive Hardness Ratios), are necessary. The assumption of a single template for all AGN is too crude to properly estimate the distribution of column densities from the GOODS sample, since particular spectral features for each source produced by soft emission or absorption can be present.

### 6.4. Highly absorbed sources and the CXRB

According to the X-Ray analysis of Seyfert II galaxies presented by Maiolino et al. (1998), the number of Compton Thick sources represents a large fraction of the AGN population. In this work, the assumption of a maximum column density at  $N_H = 10^{25} \text{ cm}^{-2}$  allows to estimate this highly absorbed population from our geometrical assumptions (see Figure 10). We roughly predict intrinsic Compton Thick source fractions of 23%, 3%, 23% and 37% for Model 1, 2, 3 and 4 respectively. When including present detection biases, using an extrapolation of Ueda's luminosity function, such as that from Figure 4, these fractions decrease roughly to 6%, 1%, 6% and 7% respectively. Present work by Tozzi & Gilli (2006) estimates an observational high luminosity fraction of more than 10% for this population using spectroscopic and photometric redshift identifications in the CDFS.

We find an essential flux contribution to the CXRB (for energies  $> 20 \text{ keV}$ ) from our predicted Compton Thick popula-

tion. However, the normalization factor,  $A$ , which is used to estimate the contribution from each source to the CXRB, can largely vary depending on the assumed reflection component for the AGN template for highly absorbed sources. This implies that a precise estimation for the intrinsic number of Compton Thick sources cannot be obtained from this analysis.

We find that even with the predicted Compton Thick sources from our torus models, the CXRB cannot be explained at  $\sim 30 \text{ keV}$ . The inclusion of a small ( $\sim 35 \text{ sources deg}^{-2}$ ) number of intrinsic local low luminosity Compton Thick sources alleviates the problem. Polletta et al. (2006) estimate a surface density of at least 25 Compton Thick AGN per square degree detected in the *Chandra*/SWIRE field. A lower value has been found by Treister et al (2006, in preparation) using 1 Msec of INTEGRAL observations in the XMM-LSS field. However, real constraints for these sources must wait for higher energy, high sensitivity, X-Ray missions, or the advent of correlations using radio, IR, and submillimetric data for AGNs.

## 7. Conclusions

1. Using the observed distribution of column densities in AGNs, and the spectral CXRB index in the  $2 - 10 \text{ keV}$  range, we have demonstrated that assuming the *Unification Model* is possible to constrain the geometry of the obscuring region present in AGNs. Four different torus geometries (see Figure 5) are constrained using KS and  $\chi^2$  tests. To compare our model predictions with the observations, we took into account detection biases explained in Subsection 3.3.

Results from our torus modeling in Section 4 are presented in Table 1. These results can be used to estimate intrinsic torus parameters, such as the inner and outer radius, and the density at the equatorial plane, as a function of the AGN luminosity.

2. An angular profile given by an exponential dependency for the matter density distribution ( $\rho$ ), such as in Model 1 and 3, gives the best estimation for the wide range of observed column densities (approximately from  $10^{20} \text{ cm}^{-2}$  to  $10^{25} \text{ cm}^{-2}$ ). Model 3 is the only model which can be compared with the reemission treatment (Granato & Danese 1994), though present clumpy torus modeling can also be applied using Equation 2 if small values for  $\tau_{Vi}$  are assumed to avoid a large dichotomy between Type I and Type II objects. A constant density distribution (Model 2) needs large scale structures to cover the observed  $N_H$ s (since  $N_H \propto \Delta s$ ), not according with actual observations of local Seyfert galaxies where pc-scale torus-like structures have been detected. We rule out a Gaussian angular dependency as proposed by Nenkova's clumpy model (Model 4), because of a substantial overestimation of highly obscured sources is predicted.
3. The analysis using the spectral index of the CXRB in the  $2 - 10 \text{ keV}$  range can constrain the fraction of Type II/I sources, but it also depends on many other fixed parameters, which can modify our estimations. Changing the Ueda et al. (2003) hard X-Ray luminosity function to that given by Barger et al. (2005) to estimate the CXRB at

< 10 keV, we obtain a negligible difference. Assuming the *Unification Model*, we found that a large fraction of Compton Thick sources are necessary to predict the CXRB at energies < 20 keV, although the presence of an extra local Compton Thick population is required to explain the hump at  $\sim 30$  keV.

For models 1 and 3, the constraints from the CXRB spectral index overlap well with  $N_H$  results, but this is not the case for the other two models.

**Acknowledgements.** This paper was supported by Proyecto MECESUP “*Expansión del Universo Astronómido en Chile*” and for GEMINI-PPARC research studentship. Thanks to E. Treister, D. Gruber, R. Wilman, D. Alexander, P. Best and R. Ivison for their data and comments for this work. P. Lira acknowledges support from Fondecyt project N° 1040719. *E.Ibar, agradece a su familia y amigos por su apoyo en todo momento, y como no también al SAJ.*

## References

Alexander, D. M., et al. 2003, AJ, 126, 539

Antonucci, R. 1993, ARA&A, 31, 473

Barger, A. J., et al. 2003, AJ, 126, 632

Barger, A. J., Cowie, L. L., Mushotzky, R. F., Yang, Y., Wang, W.-H., Steffen, A. T., & Capak, P. 2005, AJ, 129, 578

Beckert, T., & Duschl, W. J. 2004, A&A, 426, 445

Barvainis, R. 1987, ApJ, 320, 537

Bohlin, R. C., Savage, B. D., & Drake, J. F. 1978, ApJ, 224, 132

Boyle, B. J., Shanks, T., Croom, S. M., Smith, R. J., Miller, L., Loaring, N., & Heymans, C. 2000, MNRAS, 317, 1014

Comastri, A., Setti, G., Zamorani, G., & Hasinger, G. 1995, A&A, 296, 1

De Luca, A., & Molendi, S. 2004, A&A, 419, 837

Elitzur et al., 2003, astro-ph/0309040

Elitzur et al., 2005, astro-ph/0512025

Fabian, A. C., & Barcons, X. 1992, ARA&A, 30, 429

Falcke, H., Wilson, A. S., & Simpson, C. 1998, ApJ, 502, 199

Gehrels, N. 1986, ApJ, 303, 336

Giacconi, R., et al. 2002, ApJS, 139, 369

Granato, G. L., & Danese, L. 1994, MNRAS, 268, 235

Gruber, D. E., Matteson, J. L., Peterson, L. E., & Jung, G. V. 1999, ApJ, 520, 124

Hasinger, G., et al. 2001, A&A, 365, L45

Hickox, R., Markevitch, M. 2005, astro-ph/0512542

Jaffe, W., et al. 2004, Nature, 429, 47

Lightman, A. P., & Rybicki, G. B. 1980, ApJ, 236, 928

Magdziarz, P., & Zdziarski, A. A. 1995, MNRAS, 273, 837

Mainieri, V., Bergeron, J., Hasinger, G., Lehmann, I., Rosati, P., Schmidt, M., Szokoly, G., & Della Ceca, R. 2002, A&A, 393, 425

Maiolino, R., Salvati, M., Bassani, L., Dadina, M., della Ceca, R., Matt, G., Risaliti, G., & Zamorani, G. 1998, A&A, 338, 781

Markevitch, M., et al. 2003, ApJ, 583, 70

Matt, G., et al. 1999, A&A, 341, L39

Matt, G. 2002, Royal Society of London Philosophical Transactions Series A, 360, 2045

Moran, E. C., Barth, A. J., Kay, L. E., & Filippenko, A. V. 2000, ApJ, 540, L73

Moretti, A., Campana, S., Lazzati, D., & Tagliaferri, G. 2003, ApJ, 588, 696

Morrison, R., & McCammon, D. 1983, ApJ, 270, 119

Mushotzky, R., 2004, astro-ph/0405144

Nandra, K., & Pounds, K. A. 1994, MNRAS, 268, 405

Nenkova, M., Ivezić, Ž., & Elitzur, M. 2002, ApJ, 570, L9

Pier, E. A., & Krolik, J. H. 1992, ApJ, 401, 99

Pier, E. A., & Krolik, J. H. 1993, ApJ, 418, 673

Polletta, M., et al. 2006, astro-ph/0602228

Prieto, M. A., et al. 2004, ApJ, 614, 135

Prieto, M. A., Maciejewski, W., & Reunanen, J. 2005, AJ, 130, 1472

Risaliti, G., Elvis, M., Fabbiano, G., Baldi, A., & Zezas, A. 2005, ApJ, 623, L93

Ruiz, M., Rieke, G. H., & Schmidt, G. D. 1994, ApJ, 423, 608

Schultz, G. V., & Wiemer, W. 1975, A&A, 43, 133

Setti, G., & Woltjer, L. 1989, A&A, 224, L21

Spergel, D. N., et al. 2003, ApJS, 148, 175

Svensson, R. 1996, A&AS, 120, 475

Swain, M., et al. 2003, ApJ, 596, L163

Szokoly, G. P., et al. 2004, ApJS, 155, 271

Tozzi, P., Gilli, R., the CDFS Team, 2006, astro-ph/0601452

Treister, E., et al. 2004, ApJ, 616, 123

Treister, E., & Urry, C. M. 2005, ApJ, 630, 115

Ueda, Y., Akiyama, M., Ohta, K., & Miyaji, T. 2003, ApJ, 598, 886

Wilman, R. J., & Fabian, A. C. 1999, MNRAS, 309, 862

Worsley, M. A., et al. 2005, MNRAS, 357, 1281

Zakamska, N. L., Strauss, M. A., Hall, P. B., Hao, L., Ivezić, Ž., & Schlegel, D. J. 2002, Bulletin of the American Astronomical Society, 34, 1289